Research Article | Vol. 26, No. 25 | 10 Dec 2018 | OPTICS EXPRESS 32931

Optics EXPRESS

# Multi-spectral frequency selective mid-infrared microbolometers

ALIREZA SAFAEI,[1,2] SUSHRUT MODAK,[1] JONATHAN LEE,[1] SAYAN CHANDRA,[1] DANIEL FRANKLIN,[1,2] ABRAHAM VÁZQUEZ-GUARDADO,[2,3] AND DEBASHIS CHANDA[1,2,3,*]

[1]*Department of Physics, University of Central Florida, Orlando, Florida 32826, USA*
[2]*NanoScience Technology Center, University of Central Florida, Orlando, Florida 32826, USA*
[3]*CREOL, The College of Optics and Photonics, University of Central Florida, Orlando, Florida 32826, USA*
[*]*debashis.chanda@ucf.edu*

**Abstract:** Frequency selective detection of low energy photons is a scientific challenge using natural materials. A hypothetical surface which functions like a light funnel with very low thermal mass in order to enhance photon collection and suppress background thermal noise is the ideal solution to address both low temperature and frequency selective detection limitations of present detection systems. Here, we present a cavity-coupled quasi-three dimensional plasmonic crystal which induces impedance matching to the free space giving rise to extraordinary transmission through the sub-wavelength aperture array like a "light funnel" in coupling low energy incident photons resulting in frequency selective perfect (~100%) absorption of the incident radiation and zero back reflection. The peak wavelength of absorption of the incident light is almost independent of the angle of incidence and remains within 20% of its maximum (100%) up to $\theta_i \leq 45^\circ$. This perfect absorption results from the incident light-driven localized edge "micro-plasma" currents on the lossy metallic surfaces. The wide-angle light funneling is validated with experimental measurements. Further, a super-lattice based electronic biasing circuit converts the absorbed narrow linewidth ( $\Delta\lambda/\lambda_0 < 0.075$) photon energy inside the sub-wavelength thick film (< λ/100) to voltage output with high signal to noise ratio close to the theoretical limit. Such artificial plasmonic surfaces enable flexible scaling of light funneling response to any wavelength range by simple dimensional changes paving the path towards room temperature frequency selective low energy photon detection.



## 1. Introduction

Surface plasmon is collective oscillation of electrons on metal-insulator interface excited by an electromagnetic wave; the surface plasmons can be either in the propagating (surface plasmon polariton SPP) or localized surface plasmon (LSP) mode [1,2]. The fundamental order of LSP, the dipolar excitation, has the highest strength and its properties, i.e. resonance frequency and lifetime, are determined by the particle polarizability and lattice sum which depend on the metal/insulator dielectric functions and the geometrical parameters [3–6]. This dependence gives a way to control and tailor the surface plasmon resonances to desired frequencies. Surface plasmons have the potential to be used in integrated photonic circuits [1,7], SERS measurements [4], flat optics [8], hot-electron injected sensors [1,7] and metamaterials with properties such as near-zero [9], negative [10] and hyperbolic [11] index of refraction. The prime difficulty in bringing these concepts to full-fledged applications is the large plasmon decay rate mainly due to the finite metal conductivity that decreases the lifetime of the excited surface plasmon and induce losses in the form of heat dissipation [12,13]. For a long time, this loss was considered to be a major limiting factor in realization

#344263 https://doi.org/10.1364/OE.26.032931
Journal © 2018 Received 31 Aug 2018; revised 17 Oct 2018; accepted 7 Nov 2018; published 3 Dec 2018

Optics EXPRESS

of plasmonic devices but later this very loss is used as a benefit. The narrowband perfect light absorption has been shown theoretically and experimentally through critical coupling by resonant plasmonic systems [14–24]. Devices, which use narrowband plasmonic absorbers, were demonstrated for perfect metamaterial absorbers [25], spatial modulators [3,26] and narrowband infrared detection [27–39].

Here, we extend further on to the use of lossy plasmons as a mechanism of "color" sensing in infrared frequency domain by virtue of bolometric principle [33,34]. We propose quasi 3D plasmonic crystal consisting of vertically-separated complementary nanohole and nanodisk arrays coupled to an optical cavity. The general behavior of this complex system is determined by the interaction of optical cavity modes, spoof plasmonic excitation on the perforated film [40,41], hybrid plasmonic excitation on the disk array and vertical/horizontal coupling of the metallic dipolar elements, as explained by details in our previous work [3]. The purpose of exploiting mid-IR plasmon is increasing the absorption in a very small volume (low thermal mass) of the device, resulted in lower noise and higher output signal [41,42]. The geometric nature of this plasmonic crystal "funnels" the light through the subwavelength holes coupled to the disk array by exciting hybrid plasmon, which is dissipated in the form of resistive loss resulting from induced micro-currents on the edge of dipole elements (holes and disks). Surface patterning with a superlattice to sense the power dissipation with external biasing circuitry show promising results with very high spectral selectivity and response time. A 3 dB response time of 100 μs is measured, which outperforms present microbolometer's typical response time of 10-15 ms [36,37,43]. The frequency selective infrared absorption spectroscopy has proven to be a very important tool in the detection and identification of airborne chemicals by comparing infrared light absorption in presence and absence of airborne contaminants. The geometrical tunability and narrow bandwidth of the light absorption not only determines the contaminants, but also their concentration. At present both cooled and uncooled mid-infrared (mid-IR) detectors are being broadband "bucket" detectors generate integrated spectral response. Such broadband detectors are not accurate enough to perform narrow-band low concentration chemical detection from IR radiation [36,44–47]. There are quite a few IR detector concepts at the research level which are potential candidates for frequency selective detectors [18,48,49]. The proposed quasi-3D plasmonic absorber possesses inherent frequency selective detection capability paving the path towards low cost room temperature infrared "color" photon detection with high signal to noise ratio when packaged into a commercial detector architecture. The optical response of the proposed nanodevice is independent of the light polarization and angle of incidence; moreover, nanoimprinting based simple, large area and low-cost fabrication technique makes this detector realizable for the practical applications.

## 2. Quasi-3D plasmonic crystal "light funnel"

Figure. 1(a-top) schematically illustrates the proposed plasmonic crystal and the corresponding light funneling phenomenon. The quasi-3D imprinted surface is composed of a sub-wavelength perforated film and its complementary disk array with period P and diameter D, separated from the film by relief depth (RD) coupled to an optical cavity with thickness L. The composite system functions like a "light funnel" as can be observed from the 3D finite-difference time-domain (FDTD) simulation of energy flow, represented by the Poynting vector in Fig. 1(a-bottom). The simulation results show that the plane-wave incident on the top surface collapses into the subwavelength aperture like a liquid flow through a mechanical funnel, resulting in perfect capture of the incident photons at the resonance wavelength $\lambda_{res}$ = 4.4 μm for P = 1.14 μm, D = 0.760 μm, RD = 0.28 μm and L = 0.87 μm. A close correlation is observed between the simulated (solid black) and measured (solid purple) absorption spectra shown in Fig. 1(b). In order to understand the origin of the light funneling, transmission spectra of the constituent perforated film (dashed blue) and the coupled hole-disk arrays (solid blue) are overlaid in Fig. 1(b). Further, analytical coupled-dipole

Optics EXPRESS

approximation (CDA) (black dashed line) is plotted in Fig. 1(b). The good agreement of the experiment, FDTD simulation and CDA approach validates the underlying physics of the light absorption spectrum which is the temporal and spatial interaction of the coupled electric dipole arrays and the Fabry-Perot modes of the cavity as described in detailed in our separate publication [3,50].

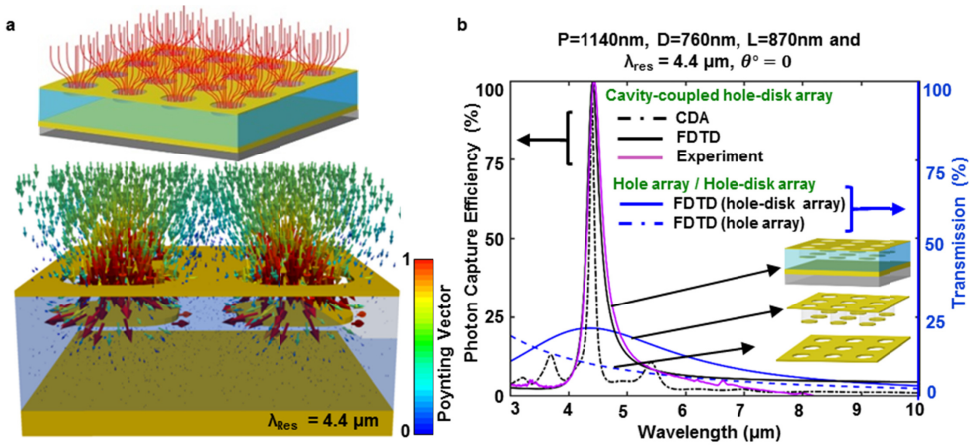


Fig. 1. Cavity-coupled quasi-3D plasmonic crystal "Light Funnel" (a) schematic illustration (top) and computed (bottom) 3D pointing vector of the incident radiation (λres = 4.4 μm). (b) Predicted transmission of the hole array (dashed-blue) and hole-disk array (blue) through the subwavelength hole and hole-disk array of period P = 1.14 μm, diameter D = 0.76 μm and relief depth RD = 280 nm. The absorption with full-wave electromagnetic simulation (black) of the cavity-coupled system along with the analytical coupled dipole approximation (CDA) prediction (black-dotted) have been overlaid for comparison for cavity thickness L = 0.87 μm (λres = 4.4 μm). The corresponding experimental verification of absorption is plotted in (purple).

The light funneling effect is almost angle independent over a wide angle of incident which can be seen from the rigorous coupled wave analysis (RCWA) simulation as well as experimental measurement in Fig. 2(a) (top and bottom respectively). The angle dependent absorption measurement is carried out in an IR integrating sphere setup which is susceptible to noise and requires long integration times for reliable data collection. Hence, a sample with larger cavity thickness (L = 1.040 μm, $\lambda_{res}$ = 4.8 μm) is chosen so the resonance is away from the carbon dioxide absorption line ($\lambda_{CO2}$ ~4.4 μm) to remove a major noise source by design. The plasmonic crystal captures energy with close to 100% efficiency across a wide angular span like a "light funnel". Beyond a steep angular range (> 60°), due to the change of dipole polarizability and the coupling between elements, a shift in the plasmon excitation wavelength of the two complementary arrays is observed. Moreover, the change in the effective cavity length detunes the combined resonance and diminishes absorption as analytically and numerically demonstrated in our earlier findings [3]. The good agreement between RCWA prediction and experimental measurement in Fig. 2(a) strongly supports the effectiveness of light funneling over wide angles of incidence.

Optics EXPRESS

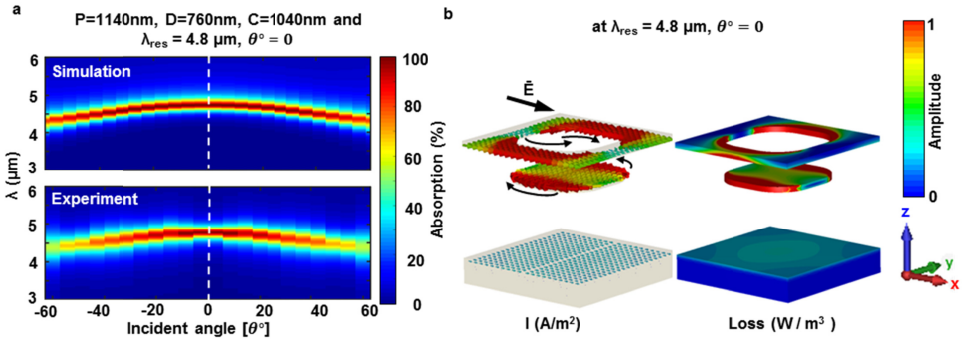


Fig. 2. Structural parameters for study of angle dependence of resonance wavelength: P = 1140nm, D = 760nm, RD = 280nm and L = 1040nm with resonance wavelength = 4.8μm. (a) (top) Rigorous coupled wave analysis (RCWA) prediction and (bottom) experimentally measured angular absorption of the plasmonic crystal (b) Current density (J) (left) and loss profile of the metal (right) at resonance wavelength.

CST Microwave Studio and FDTD, Lumerical inc. were used for electromagnetic simulations. Dispersion for gold is obtained by fitting Palik's experimental data [51] with Drude model, and refractive index of SU-8 is considered as 1.56. To accurately perform simulations for the samples, which were fabricated, exact values of diameter and the rounding radius of hole is obtained from SEM images. Angle dependent rigorous coupled-wave analysis (RCWA, GD Cal) simulations were conducted with a custom-built MATLAB script to understand the angle dependent behavior of the structure due to the limitations of FDTD method for oblique angles of incidence. To measure the absorption spectra of the sample for the normal incident light, a 2.5x, 0.07 numerical aperture IR transparent ZnSe objective lens on an optical microscope (Hyperion 1000) coupled to a Fourier transform infrared (FTIR) spectrometer (Vertex 80, Bruker Corp.) and a mercury cadmium telluride (MCT) photodetector was used. Since the MCT photodetector is cryogenically cooled, it offers much higher signal to noise ratio and hence needs lower integration time. This setup is designed just for characterization of normal angle of incidence. In order to quantify the wavelength dependent absorption for non-normal angle of incidence a special gold coated integrating sphere (Bruker Inc.) coupled to a FTIR spectrometer is used. The integrating sphere has its own room temperature bolometer to detect the scattered photons. Since bolometer has higher noise compared to the cryogenic detector, we increased the integration time (10 min) to obtain reflection spectrum with lower noise. Reflection spectra were normalized to a gold mirror with 96% reflectivity over the wavelengths examined.

## 3. Plasmon loss mechanism

An analysis of the fields inside the composite structure reveals the absorption and subsequent dissipation mechanisms [Fig. 2(b)]. The incident plane-wave induces in-phase charge oscillations, localized surface plasmon (LSP), in the direction of the electric field around the edges of the holes on the top surface [Fig. 2(b-left)]. The near-field coupling induces complementary charge oscillations (coupled LSP) in the disc concentrated around the edges. In the presence of a mirror at a distance L the charge oscillations and the electric dipole magnitude on the disk array are reinforced due to the electric field antinode in the center of the cavity ($L_{eff} = (2m+1)\lambda / 2n_{eff}$). The reinforced charge oscillations on the disc-array in turn increase the near field coupling with the hole-array (positive feedback) leading to the transmission enhancement with 100% coupling efficiency and the funneling behavior of the structure. The strength of the positive feedback depends on two factors- the strength of near field coupling between holes and disk (hence the distance between them) and the position of the disk array in the cavity, i.e., the intensity of electric field 'seen' by the disc array.

Optics EXPRESS

Moreover, the lateral coupling between the disk and hole-array is also important for the high amplitude of absorption. Increase in the distance between elements decreases the coupling between them, which in turn reduces the total absorption in the structure. Increasing the angle effectively reduces the effective pattern period and red shifts the resonance. At the same time, the effective distance between the hole and disk is increased compared to the period, which in turn blue shifts the resonance (dominant effect) and the overall coupling strength diminishes as well. This is verified in Fig. 2(a-top) (angle dependent RCWA simulation) and Fig. 2(a-bottom) (angular measurements).

The bulk of the light is absorbed along the edges of hole and disc array as seen from Fig. 2(b-right) and it is important to understand the reason behind this phenomenon. The discs are part of a lattice composed of discrete elements and the Coulomb interaction with the neighboring discs force the induced charges on the discs to move to the edges but more predominantly to the corners. Counter-propagating LSP on the edges of hole and disk form a magnetic dipole and one pair of hole-disk supports two such magnetic dipoles on opposite edges [Fig. 2(b-left)]. The localized nature of the current density on hole-disc is responsible for the paired magnetic dipoles to incur high Ohmic losses $P = \mathbf{J}.\mathbf{E}$, where $\mathbf{J}$ is the current density; $\mathbf{E}$ is the electric field and $P$ is the loss power density). The simulated 3D current distribution is shown in Fig. 2(b-left) which clearly verifies the origin of the photon capture and dissipation on the edges of the hole-disk as observed in Fig. 2(b-right).

## 4. Light detection

Ideal surface plasmons with zero damping have many interesting properties like near-zero index and infinite phase velocity which are theoretically predicted [52–54] but the translation of these ideas into practical realm is limited due to the inherent losses in metals that are used to fabricate such structures. In most applications, the presence of metal is not desirable due to the loss; however, sensing applications can take advantage of the plasmon damping and plasmon-phonon coupling to sense change in the electrical conductivity. In this proposed system, the change in resistance of the plasmonic crystal due to the absorbed electromagnetic radiation is measured with the help of a DC biasing circuit. Schematic illustration of the circuit is shown in Figs. 3(a) and 3(b). The scanning electron microscopy image of the fabricated super-lattice is shown in Fig. 3(c). The circuit uses a simple voltage divider scheme to bias the detector [Fig. 3(d)]. The plasmonic film absorbs the incident radiation and produces thermal energy which in turn manifests in the form of resistance change. The continuous perforated film enables electronic probing of the induced "micro-current" plasmon loss on each nanohole via the weak bias current ($I_B$). The input impedance is increased from a few ohms to kilo-ohm range with the superposition of a serpentine super-lattice pattern to amplify the resistive change ($\Delta R \approx R_D \alpha \Delta T$, where $R_D$ is the detector resistance at room temperature, $\alpha$ is the thermal coefficient of resistance and $\Delta T$ is the induced temperature change due to absorbed radiation) and reduce the background heating (Joule heating [28,33,36,37]) due to the bias current.

As seen from the SEM images in Fig. 3(c), the device consists of the gold serpentine absorber with hole-disk nanopattern supported by a polymer base (SU-8 2000.5). A gold mirror on glass substrate supports the polymer. In this manner, the polymer acts as the cavity dielectric, moreover, the polymer curing process minimizes and makes the absorption in the polymer negligible. Large area (4 mm x 4 mm) square arrays of subwavelength cylindrical depressions were molded onto the surface of a thin layer of a photo curable epoxy (SU-8 2000.5, MicroChem), by pressing the substrate against a polydimethylsiloxane (PDMS, 10:1 Sylgard 184) mold containing the inverse pattern. The thickness of the epoxy was controlled through the spin-coating process. A gold-coated microscope glass slide served as the substrate. To form the detector super-lattice serpentine pattern, after imprinting, a prolonged UV exposure (30 min) and post exposure bake (95 deg for 60 min) was conducted to make SU-8 fully cross-linked to make it resistant to acetone during subsequent liftoff process. A

Optics EXPRESS

UV lithography step was performed on top of this imprinted array of holes followed by blanket deposition of gold (~30 nm) and lift-off process to form serpentine layout with contact pads to facilitate electrical measurements. The size of serpentine pattern is 1 mm x 1 mm and width of each line in the serpentine pattern is 25 µm for the present design. A conductive silver epoxy is used to attach wires to the contact pads for electrical interfacing with measurement setup.

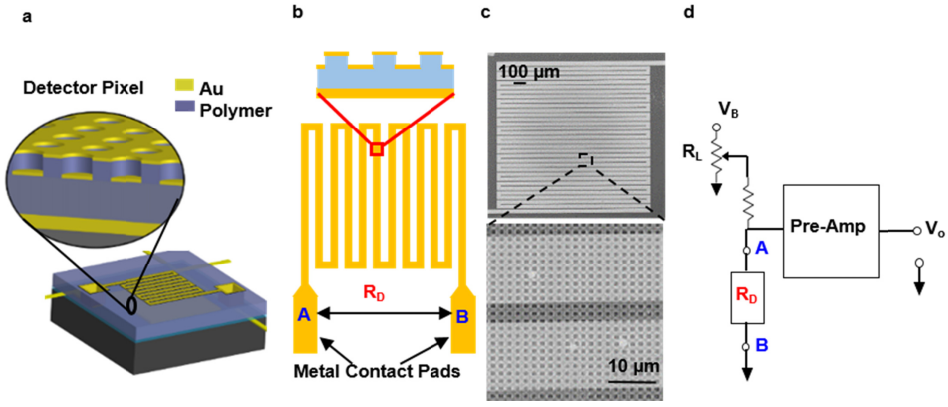


Fig. 3. (a) 3D cartoon depicting the structure of the detector, (b) upper gold film formatted in the form of a serpentine pattern (superlattice) to form a path with significant resistance and contact pads for interfacing with external biasing circuit (c) SEM image of the fabricated detector with hole-disk nano-pattern and gold film in the form of serpentine pattern and (d) interfacing circuit in voltage divider bias mode, as used in the experiments.

The super-lattice pattern plays the important role of enhancing the signal to noise ratio albeit bit reduction (~5%) in overall photon capture efficiency due to the reduction in active area. The plasmonic surface with D = 0.760 µm, P = 1.14 µm and the gold thickness of 30 nm results in ~4 ohm/mm$^2$ resistance which is increased to ~7k ohm/ mm$^2$ with the serpentine pattern with 25 µm width and 85% duty cycle. The schematic of the measurement circuit is shown in Fig. 3(d).

The measured photon capture/absorption spectra of three fabricated spectrally selective plasmonic infrared detectors are plotted along with the normalized black body radiation at T = 1200° C in Fig. 4(a). The spectral detuning of detectors ($\lambda_1$ = 4.2 µm, $\lambda_2$ = 4.5 µm and $\lambda_3$ = 4.8 µm) is achieved through cavity thickness variation ($L_1$ = 0.760 µm, $L_2$ = 0.920 µm and $L_3$ = 1.040 µm) for constant diameter, D = 0.760 µm and period, P = 1.14 µm. The corresponding measured voltage change ($\Delta V_o$) divided by the respective detector electrical resistance $\Delta V_o/R_m$ as a function of bias current for the three narrowband (FWHM ~300 nm) frequency selective plasmonic detectors at ambient temperature and pressure are shown in Fig. 4(b). The signal voltage is normalized with respect to the detector resistance to remove the effect of detector-to-detector resistance variation from the results. The normalized voltage scales according to the absorbed incident power at the absorption wavelength for a given source temperature. Such spectrally resolved detection is not possible with the conventional broadband bucket detectors. A measure of the sensitivity of a radiation sensor is calculated from its noise equivalent power (NEP). Out of the various noise sources such as photon noise, thermal fluctuation noise, 1/f noise and thermal noise; resistive detector like this one have thermal noise (Johnson noise) as the dominant source of noise which is directly proportional to the square root of the resistance of the sensor [44,47].

The figure of merit of a detector that considers NEP, detector area ( $A$ ) and bandwidth ( $\Delta f$ ) of operation is specific detectivity $D_{FS}^*$ ( $D^* = \sqrt{A\Delta f} / NEP$ cm$\sqrt{\text{Hz}}$/W), the suffix '$FS$' stands for frequency selective in order to distinguish it from the traditional D* of broadband detectors). A Simulink model is developed to solve the heat equations for the current device

Optics EXPRESS

architecture to understand its theoretical performance limits and emulate the thermal equations for a given device geometry. It takes geometric parameters of the device, thermal and electrical constants of the constituent materials, incident radiation power and the chopping frequency as the input parameters to generate the time dependent voltage response and time constant.

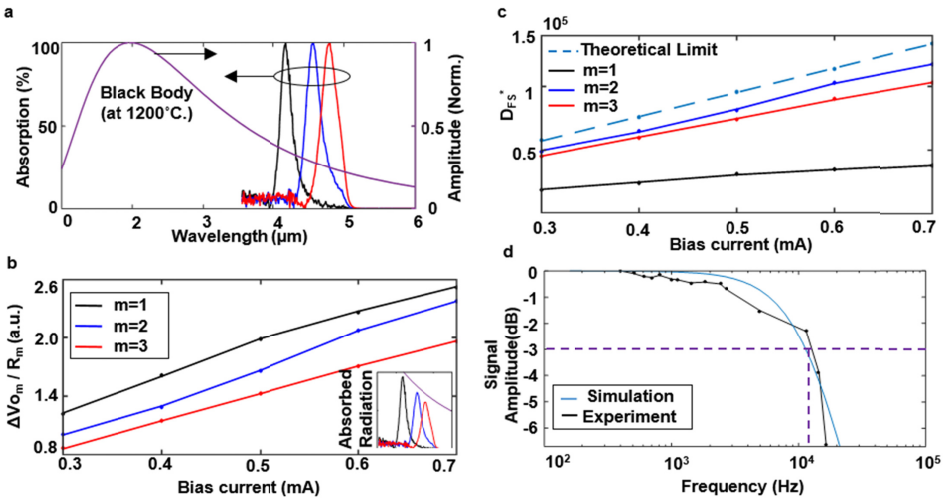


Fig. 4. (a) Normalized black-body spectrum along with frequency selective absorption spectra of three detectors at 4.2 μm (m = 1), 4.5 μm (m = 2) and 4.8 μm (m = 3). (b) Normalized detector output $\Delta V_m/R_m$ for m = 1 to 3. Inset shows the absorbed incident power of the detectors at a constant source temperature of 1200°C. The individual detector response follows the absorbed incident power. (c) Predicted (with Simulink model) and measured specific detectivity of the frequency selective detectors. (d) Simulated (dotted blue) and measured (with $3\omega$ method) detector frequency response. The measured 3 dB roll-off indicates a response time of 100 μs.

The simulated detectivity and time response are plotted in Figs. 4(c) and 4(d), respectively. Thermal noise limited measured detectivity of three detectors as a function of bias current is plotted in Fig. 4(c). The measured $D_{FS}$* of the three frequency-selective plasmonic detectors closely follow the theoretical limit. The measured frequency selective D* for the present case is not directly comparable to cooled or uncooled broadband IR detectors due to their broadband energy absorption, as the signal and the noise generation processes both depend on the bandwidth [35]. Further, the frequency response of the detector is measured with AC electrical $3\omega$ method [28,55–57] and is plotted in Fig. 4(d). A 3 dB response time of 100 μs is measured which outperforms present microbolometers response time of 10-15 ms [36,37,43]. Present commercially available suspended Vanadium Oxide ($VO_x$) based microbolometers response time ranges between 6 and 20 ms (European space agency; FLIR) with the responsivity of 600 kV/W. In addition, ULIS Inc. reported a time response of 2.5 ms which is the record for the commercial high-sensitive room temperature microbolometers. The short surface plasmon life time (~$10^{-15}$s) [1] and extremely fast thermal dissipation (~$10^{-9}$s) [13] due to the ultra-low thermal mass makes plasmonic detectors on the faster side compared to bulk absorption based thermal detectors. Further design optimization with reduction in thermal conductivity based on a suspended detector architecture, partial vacuum seal and electrical noise reduction following well-known commercial IR detector fabrication procedures will drastically improve the present frequency selective plasmonic detector signal to noise ratio (D* ~$10^8$ - $10^9$ cm.√Hz /W) [44,45,47]. The bolometers made from perforated gold on ZnO can reach to the maximum responsivity of $R_{max}$ = 10 mV/W which is smaller than our value ($R_{max}$≈15 mV/W) [15]. Single nanowire-based infrared

Optics EXPRESS

bolometer is reported to possess the responsivity of $R_{max}$ = 70 mV/W, but it lacked the spectral tunability. Excitation of plasmon on gold nanowire sitting on $SiO_2$ can increase the $R_{max}$ to 400 mV/W, at the cost of polarization dependency and complex fabrication steps [58]. The proposed detector when fabricated in a suspended architecture can reach to higher responsivity and D*. The predicted responsivity of the suspended proposed microbolometer working at room temperature is $R_{max}$ ≈1 kV/W - 10 kV/W, D*≈5 × $10^7$ cmHz$^{1/2}$W$^{-1}$ - 2 × $10^9$ cmHz$^{1/2}$W$^{-1}$, while the time constant is τ = 0.5 ms - 1s for a similar pixel dimension [59–61].

## 5. Conclusion

In conclusion, the proposed plasmonic nanostructure demonstrates a new mechanism to enhance and engineer light-matter interactions. The excitation of surface plasmon on the hole/disk array due to the presence of the optical cavity enhances the photon capture to ~100%. The coupling between two complementary metallic elements can be varied flexibly to shift the resonance location and strength. Tunability can also be exploited from the cavity phase relation, which can be simply tuned with cavity thickness. Metal based plasmonic nanostructures suffer from metallic loss, but here we take advantage of such a high resistive loss for the detection of photons. Such controlled infrared absorption when implemented in conjunction with simple large area imprinting techniques leads to development of a new class of frequency selective, low cost, uncooled infrared detectors. Our initial studies presented above have shown that a frequency selective plasmonic surface can alleviate some of the limitations of present IR detectors and offer significant improvements in frequency selective detection paving the path towards IR "color" imaging by pixel/sub-pixel formation with plasmonic surfaces tuned to various IR bands.

## Funding

Florida Space Institute/NASA FSGC (grant no. 63019022); Northrop Grumman Mission Systems' University Research Program; and DARPA under the WIRED program (Grant No. HR0011-16-1-0003).

## Author contributions

D.C. conceived the idea. D.C. designed and S.M. performed the experiments. A.S., D.F., and A.V.G. provided technical guidance. A.S. and S.M. analyzed and simulated the data. S.M. and S.C. performed measurements. A.S., S.M. and D.C. cowrote the paper.

## Disclosures

The authors declare no competing financial interests.

## Acknowledgments

We gratefully acknowledge the contribution of Dr. Augustine Urbas who carried out the IR ellipsometric measurements of refractive indices at Airforce Research Laboratory, Dayton, Ohio.

## References

1. H. Paudel, A. Safaei, and M. Leuenberger, "Nanoplasmonics in Metallic Nanostructures and Dirac Systems" (IntechOpen, 2017) Chap 3.
2. S. A. Maier, *Plasmonics: Fundamentals and Applications* (Springer, 2007).
3. S. Modak, A. Safaei, and D. Chanda, Cavity Induced Tunable Extraordinary Transmission: A Unique Way of Funneling Light through Subwavelength Apertures." ArXiv e-prints 2017; https://ui. adsabs.harvard.edu/ #abs/2017arXiv171000392M (accessed October 01, 2017).
4. F. J. García de Abajo, "Colloquium: Light scattering by particle and hole arrays," Rev. Mod. Phys. **79**(4), 1267–1290 (2007).
5. A. Safaei, S. Chandra, A. Vázquez-Guardado, J. Calderon, D. Franklin, L. Tetard, L. Zhai, M. N. Leuenberger, and D. Chanda, "Dynamically tunable extraordinary light absorption in monolayer graphene," Phys. Rev. B **96**(16), 165431 (2017).

Optics EXPRESS


6. A. Safaei, S. Chandra, M. N. Leuenberger, and D. Chanda, "Wide Angle Dynamically Tunable Enhanced Infrared Absorption on Large Area Nanopatterned Graphene." ArXiv e-prints 2018; http://adsabs.harvard.edu/abs/2018arXiv180600837S (accessed Jun 03, 2018).
7. M. L. Brongersma, N. J. Halas, and P. Nordlander, "Plasmon-induced hot carrier science and technology," Nat. Nanotechnol. **10**(1), 25–34 (2015).
8. A. Safaei, A. Vázquez-Guardado, D. Franklin, M. N. Leuenberger, and D. Chanda, "High-Efficiency Broadband Mid-Infrared Flat Lens," Adv. Opt. Mater. **6**(13), 1800216 (2018).
9. W. D. Newman, C. L. Cortes, J. Atkinson, S. Pramanik, R. G. DeCorby, and Z. Jacob, "Ferrell–Berreman Modes in Plasmonic Epsilon-near-Zero Media," ACS Photonics **2**(1), 2–7 (2015).
10. R. de Waele, S. P. Burgos, H. A. Atwater, and A. Polman, "Negative refractive index in coaxial plasmon waveguides," Opt. Express **18**(12), 12770–12778 (2010).
11. F. Peragut, L. Cerutti, A. Baranov, J. P. Hugonin, T. Taliercio, Y. De Wilde, and J. J. Greffet, "Hyperbolic metamaterials and surface plasmon polaritons," Optica **4**(11), 1409–1415 (2017).
12. A. M. Brown, R. Sundararaman, P. Narang, W. A. Goddard 3rd, and H. A. Atwater, "Nonradiative plasmon decay and hot carrier dynamics: effects of phonons, surfaces, and geometry," ACS Nano **10**(1), 957–966 (2016).
13. R. Sundararaman, P. Narang, A. S. Jermyn, W. A. Goddard 3rd, and H. A. Atwater, "Theoretical predictions for hot-carrier generation from surface plasmon decay," Nat. Commun. **5**(1), 5788 (2014).
14. T. D. Dao, K. Chen, S. Ishii, A. Ohi, T. Nabatame, M. Kitajima, and T. Nagao, "Infrared perfect absorbers fabricated by colloidal mask etching of Al–Al2O3–Al trilayers," ACS Photonics **2**(7), 964–970 (2015).
15. T. D. Dao, S. Ishii, T. Yokoyama, T. Sawada, R. P. Sugavaneshwar, K. Chen, Y. Wada, T. Nabatame, and T. Nagao, "Hole array perfect absorbers for spectrally selective midwavelength infrared pyroelectric detectors," ACS Photonics **3**(7), 1271–1278 (2016).
16. Y. Nishijima, A. Balčytis, S. Naganuma, G. Seniutinas, and S. Juodkazis, "Tailoring metal and insulator contributions in plasmonic perfect absorber metasurfaces," ACS Applied Nano Materials **1**(7), 3557–3564 (2018).
17. J. Rosenberg, R. V. Shenoi, S. Krishna, and O. Painter, "Design of plasmonic photonic crystal resonant cavities for polarization sensitive infrared photodetectors," Opt. Express **18**(4), 3672–3686 (2010).
18. J. Rosenberg, R. V. Shenoi, T. E. Vandervelde, S. Krishna, and O. Painter, "A multispectral and polarization-selective surface-plasmon resonant midinfrared detector," Appl. Phys. Lett. **95**(16), 161101 (2009).
19. T. Gu, A. Andryieuski, Y. Hao, Y. Li, J. Hone, C. W. Wong, A. Lavrinenko, T. Low, and T. F. Heinz, "Photonic and plasmonic guided modes in graphene–silicon photonic crystals," ACS Photonics **2**(11), 1552–1558 (2015).
20. J. K. Yang, M.-K. Seo, I. K. Hwang, S. B. Kim, and Y. H. Lee, "Polarization-selective resonant photonic crystal photodetector," Appl. Phys. Lett. **93**(21), 211103 (2008).
21. X. Hu, M. Li, Z. Ye, W. Y. Leung, K.-M. Ho, and S. Y. Lin, "Design of midinfrared photodetectors enhanced by resonant cavities with subwavelength metallic gratings," Appl. Phys. Lett. **93**(24), 241108 (2008).
22. J. S. White, G. Veronis, Z. Yu, E. S. Barnard, A. Chandran, S. Fan, and M. L. Brongersma, "Extraordinary optical absorption through subwavelength slits," Opt. Lett. **34**(5), 686–688 (2009).
23. Q. Feng, M. Pu, C. Hu, and X. Luo, "Engineering the dispersion of metamaterial surface for broadband infrared absorption," Opt. Lett. **37**(11), 2133–2135 (2012).
24. S. Chandra, D. Franklin, J. Cozart, A. Safaei, and D. Chanda, "Adaptive multispectral infrared camouflage," ACS Photonics **5**(11), 4513–4519 (2018).
25. N. I. Landy, S. Sajuyigbe, J. J. Mock, D. R. Smith, and W. J. Padilla, "Perfect metamaterial absorber," Phys. Rev. Lett. **100**(20), 207402 (2008).
26. D. Li and D. Pacifici, "Strong amplitude and phase modulation of optical spatial coherence with surface plasmon polaritons," Sci. Adv. **3**(10), e1700133 (2017).
27. A. S. Gawarikar, R. P. Shea, and J. J. Talghader, "High detectivity uncooled thermal detectors with resonant cavity coupled absorption in the long-wave infrared," IEEE Trans. Electron Dev. **60**(8), 2586–2591 (2013).
28. F. B. P. Niesler, J. K. Gansel, S. Fischbach, and M. Wegener, "Metamaterial metal-based bolometers," Appl. Phys. Lett. **100**(20), 203508 (2012).
29. J. Y. Suen, K. Fan, J. Montoya, C. Bingham, V. Stenger, S. Sriram, and W. J. Padilla, "Multifunctional metamaterial pyroelectric infrared detectors," Optica **4**(2), 276–279 (2017).
30. D. D. Coon, R. P. G. Karunasiri, and L. Z. Liu, "Narrow band infrared detection in multiquantum well structures," Appl. Phys. Lett. **47**(3), 289–291 (1985).
31. Z. Qian, S. Kang, V. Rajaram, and M. Rinaldi, "Narrowband MEMS resonant infrared detectors based on ultrathin perfect plasmonic absorbers," 2016 IEEE SENSORS, **1**, 16597228 (2016).
32. G. C. Dyer, G. R. Aizin, J. L. Reno, E. A. Shaner, and S. J. Allen, "Novel tunable millimeter-wave grating-gated plasmonic detectors," IEEE J. Sel. Top. Quantum Electron. **17**(1), 85–91 (2011).
33. G. C. Dyer, J. D. Crossno, G. R. Aizin, E. A. Shaner, M. C. Wanke, J. L. Reno, and S. J. Allen, "A plasmonic terahertz detector with a monolithic hot electron bolometer," J. Phys. Condens. Matter **21**(19), 195803 (2009).
34. M. Mahjouri-Samani, Y. S. Zhou, X. N. He, W. Xiong, P. Hilger, and Y. F. Lu, "Plasmonic-enhanced carbon nanotube infrared bolometers," Nanotechnology **24**(3), 035502 (2013).
35. J. J. Talghader, A. S. Gawarikar, and R. P. Shea, "Spectral selectivity in infrared thermal detection," Light Sci. Appl. **1**(8), e24 (2012).
36. K. C. Liddiard, "Thin-film resistance bolometer ir detectors," Infrared Phys. **24**(1), 57–64 (1984).

Optics EXPRESS


37. F. Niklaus, C. Jansson, A. Decharat, J.-E. Källhammer, H. Pettersson, and G. Stemme, "Uncooled infrared bolometer arrays operating in a low to medium vacuum atmosphere: performance model and tradeoffs," in *Infrared Technology and Applications XXXIII*, (SPIE, 2007)
38. D. Chanda, A. Safaei, and M. N. Leuenberger, "Optical detector device with patterned graphene layer and related methods," US Patent App. 15/782,948 (2018).
39. D. Chanda, S. Modak, J. Lee, and A. Safaei, "Optical frequency-selective absorber-based infrared detector, methods, and applications," US Patent App. 15/538,746 (2018).
40. J. B. Pendry, L. Martín-Moreno, and F. J. Garcia-Vidal, "Mimicking surface plasmons with structured surfaces," Science **305**(5685), 847–848 (2004).
41. R. Stanley, "Plasmonics in the mid-infrared," Nat. Photonics **6**(7), 409–411 (2012).
42. P. Bouchon, F. Pardo, B. Portier, L. Ferlazzo, P. Ghenuche, G. Dagher, C. Dupuis, N. Bardou, R. Haïdar, and J. L. Pelouard, "Total funneling of light in high aspect ratio plasmonic nanoresonators," Appl. Phys. Lett. **98**(19), 191109 (2011).
43. R. Wood, *Monolithic Silicon Microbolometer Arrays*, Uncooled Infrared Imaging Arrays and Systems (Academic, 1997), Vol. **47**.
44. E. L. Dereniak and G. D. Boreman, *Infrared Detectors and Systems* (John Wiley & Sons, Inc., 1996).
45. A. Rogalski, "Infrared detectors: an overview," Infrared Phys. Technol. **43**(3-5), 187–210 (2002).
46. A. Rogalski, J. Antoszewski, and L. Faraone, "Third-generation infrared photodetector arrays," J. Appl. Phys. **105**(9), 091101 (2009).
47. P. W. Kruse, Uncooled thermal imaging: arrays, systems, and applications / Paul W. Kruse, Tutorial texts in optical engineering: v. TT 51 (Bellingham, Wash., USA, SPIE 2001).
48. S. D. Gunapala, S. V. Bandara, J. K. Liu, J. M. Mumolo, S. B. Rafol, D. Z. Ting, A. Soibel, and C. Hill, "Quantum Well Infrared Photodetector Technology and Applications," IEEE J. Sel. Top. Quantum Electron. **20**(6), 154–165 (2014).
49. D. M. T. Kuo, A. B. Fang, and Y. C. Chang, "Theoretical modeling of dark current and photo-response for quantum well and quantum dot infrared detectors," Infrared Phys. Technol. **42**(3-5), 433–442 (2001).
50. A. Vázquez-Guardado, A. Safaei, S. Modak, D. Franklin, and D. Chanda, "Hybrid coupling mechanism in a system supporting high order diffraction, plasmonic, and cavity resonances," Phys. Rev. Lett. **113**(26), 263902 (2014).
51. E. D. Palik, *Handbook of Optical-Constants* (Academic, 1984).
52. R. W. Ziolkowski, "Propagation in and scattering from a matched metamaterial having a zero index of refraction," Phys. Rev. E Stat. Nonlin. Soft Matter Phys. **70**(4), 046608 (2004).
53. E. J. R. Vesseur, T. Coenen, H. Caglayan, N. Engheta, and A. Polman, "Experimental verification of n = 0 structures for visible light," Phys. Rev. Lett. **110**(1), 013902 (2013).
54. A. M. Mahmoud and N. Engheta, "Wave-matter interactions in epsilon-and-mu-near-zero structures," Nat. Commun. **5**(1), 5638 (2014).
55. J. C. Mather, "Electrical self-calibration of nonideal bolometers," Appl. Opt. **23**(18), 3181–3183 (1984).
56. M. Ou-Yang, C. S. Sheen, and J. S. Shie, "Parameter extraction of resistive thermal microsensors by AC electrical method," IEEE Trans. Instrum. Meas. **47**(2), 403–408 (1998).
57. Y. M. Chen, J. S. Shie, and T. Hwang, "Parameter extraction of resistive thermal sensors," Sens. Actuators A Phys. **55**(1), 43–47 (1996).
58. J. B. Herzog, M. W. Knight, and D. Natelson, "Thermoplasmonics: quantifying plasmonic heating in single nanowires," Nano Lett. **14**(2), 499–503 (2014).
59. U. Dillner, E. Kessler, and H. G. Meyer, "Figures of merit of thermoelectric and bolometric thermal radiation sensors," Journal of Sensors and Sensor Systems **2**(1), 85–94 (2013).
60. A. Varpula, A. V. Timofeev, A. Shchepetov, K. Grigoras, J. Hassel, J. Ahopelto, M. Ylilammi, and M. Prunnila, "Thermoelectric thermal detectors based on ultra-thin heavily doped single-crystal silicon membranes," Appl. Phys. Lett. **110**(26), 262101 (2017).
61. G. Wang, V. Yefremenko, V. Novosad, J. Pearson, R. Divan, C. L. Chang, L. Bleem, A. T. Crites, J. Mehl, B. A. Benson, T. Natoli, K. Story, S. S. Meyer, J. E. Carlstrom, J. McMahon, J. Sayre, J. Ruhl, E. George, N. Harrington, C. Reichardt, E. Shirokoff, E. Young, A. Lee, and W. Holzapfel, "An Absorber-coupled TES Bolometer for Measuring CMB Polarization," Phys. Procedia **37**, 1349–1354 (2012).